

How non-stationary are moderately supercritical shocks?

Michael Gedalin[†]

Department of Physics, Ben-Gurion University of the Negev, Beer-Sheva, Israel

(Received 20 July 2019; revised 18 September 2019; accepted 19 September 2019)

Ion motion in a collisionless shock front is affected by macroscopic large-scale weakly varying and microscopic small-scale fast varying magnetic and electric fields. With the increase of the Mach number the role of the microscopic field is expected to become progressively more important. Using a combination of hybrid simulations and test particle analysis, we show that in moderately supercritical shocks macroscopic fields play the main role in ion motion across the shock. Pressure balance across the shock is only weakly broken and non-stationarity is related to the deviations from the total pressure from the constant value.

Key words: space plasma physics

1. Introduction

Ion motion in a magnetized collisionless shock front is affected by macroscopic large-scale weakly varying and microscopic small-scale fast-varying magnetic and electric fields. Low Mach number low- β shocks are nearly one-dimensional and stationary (Greenstadt *et al.* 1975; Greenstadt *et al.* 1980; Russell *et al.* 1982; Mellott & Greenstadt 1984; Farris, Russell & Thomsen 1993), so that time dependency and wave activity are weak (see, however, Wilson III *et al.* (2017)). Therefore, one can expect that in low Mach number shocks macroscopic fields dominate. With the increase of the Mach number shocks become more time dependent and wave activity increases. By time dependence we mean here non-stationarity of the shock structure at spatial scales of the ramp and larger and temporal scales of the order of the ion gyroperiod, while wave activity may refer to any feature of a smaller spatial and/or temporal scale. High Mach number shocks are expected to be reforming (Greenstadt *et al.* 1975; Scudder *et al.* 1986; Newbury, Russell & Gedalin 1998; Krasnoselskikh *et al.* 2002; Scholer & Matsukiyo 2004; Burgess & Scholer 2007; Lobzin *et al.* 2007; Scholer & Burgess 2007; Lobzin *et al.* 2008; Lembège *et al.* 2009; Yang *et al.* 2009; Mazelle *et al.* 2010; Umeda *et al.* 2010; Comişel *et al.* 2011; Kajdič *et al.* 2012; Wilson *et al.* 2012; Dimmock *et al.* 2019). In such shocks the macroscopic fields become essentially time dependent, in addition to strong microscopic fields. When a shock Mach number exceeds the critical value, resistivity and thermal conduction can no longer sustain the shock profile (Coroniti 1970; Edmiston & Kennel 1984; Kennel 1987).

[†] Email address for correspondence: gedalin@bgu.ac.il

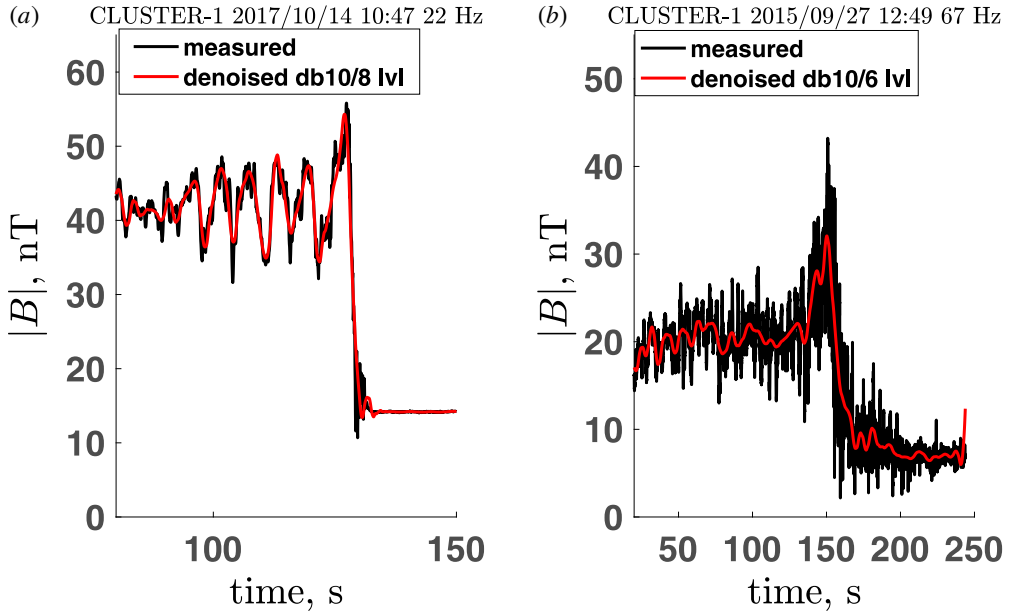


FIGURE 1. Two shocks observed by CLUSTER.

Supercritical shocks have structured profiles (Newbury, Russell & Gedalin 1998) and ion reflection is expected to play an important role. For moderately supercritical shocks time dependence of macroscopic fields is still weak while the amplitude of microscopic fields rapidly increases with the increase of the Mach number. One therefore could expect that in higher Mach number shocks the role of microscopic fields becomes progressively more important. Until now relative influence of the macroscopic and microscopic fields on ion motion has not been analysed quantitatively. Figure 1 illustrates what we mean by macroscopic and microscopic fields. The figure presents magnetic profiles, $|B|$, measured at two bow shock crossings by CLUSTER. The measured profiles are shown in black. The red curves are the profiles with the microscopic fields removed. The removal was done by applying discrete wavelet transform, removing a number of finest levels and further applying inverse transform (Kumar & Foufoula-Georgiou 1997; Gedalin, Newbury & Russell 1998; Torrence & Compo 1998; Gedalin, Newbury & Russell 2000). Daubechies 10 wavelet was used in both cases. The magnetic field in (a) is measured with the sampling rate of 22 Hz. The 2^{12} point data were processed and the 8 lowest levels were retained. Panel (b) has sampling rate of 67 Hz, 2^{14} points, and 6 levels retained. The higher is the sampling rate the more fluctuations are measured and stronger denoising is required to remove these fluctuations. The difference between the black and red curves is what is called here the microscopic fields. Denoising is not unambiguous and, in principle, should be verified *a posteriori* in an indirect way, by analysing consequences of the cleaning for the processes in the shock and comparing with observations. Here figure 1 is for illustrative purposes only. As a side note: the small-scale fluctuations in (b) resemble the waves generated by the ramp and propagating to both directions, as argued by Granit & Gedalin (2018). This is only a speculation at this stage though.

To summarize, we distinguish between the possibly time-dependent macroscopic field (the red curves in figure 1) and the presumably fast time/space-varying

microscopic fields. The first will be also referred to as a non-stationary shock structure while the latter will be referred to as fluctuations. The objective of the present paper is to establish whether macroscopic fields still dominate ion motion even when these fields become time dependent. If yes, to what extent does the relation of the ion motion to the magnetic field change?

2. The framework

In the absence of binary collisions, the motion of each charged particle within the shock front is governed by the total self-consistent electric and magnetic fields which are, in general, space and time dependent. Knowing these fields one could, in principle, find the distribution functions of all charged particles. The latter would provide the charge and current densities and the fields themselves via Maxwell's equations. It is not possible at present to have a self-consistent solution of the kinetic (Vlasov) and Maxwell equations. It is possible to simplify the problem using reasonable assumptions and to seek solutions which are partially self-consistent. Since the best available *in situ* measurements at shocks are magnetic field measurements in the heliosphere, we focus on the relation of the particle motion to the magnetic field. The magnetic field can be regarded as shaped by particles via the momentum conservation laws

$$\frac{\partial}{\partial t} \left(\sum_s n_s m_s \mathbf{V}_{s,i} \right) + \frac{\partial}{\partial x_j} \left(\sum_s P_{s,ij} + \frac{B^2 \delta_{ij}}{8\pi} - \frac{B_i B_j}{4\pi} \right) = 0. \tag{2.1}$$

Here s denotes species (electrons, protons, alpha particles); $i, j = x, y, z$ and δ_{ij} is the Kronecker tensor. The density, hydrodynamical velocity and total pressure tensor are defined using the distribution function,

$$n_s = \int f_s(\mathbf{r}, t, \mathbf{v}) d^3 \mathbf{v}, \tag{2.2}$$

$$n_s V_{s,i} = \int v_i f_s(\mathbf{r}, t, \mathbf{v}) d^3 \mathbf{v}, \tag{2.3}$$

$$P_{s,ij} = \int m_s v_i v_j f_s(\mathbf{r}, t, \mathbf{v}) d^3 \mathbf{v}. \tag{2.4}$$

The total pressure includes both dynamic pressure $P_{\text{dyn},ij} = nmV_i V_j$ and kinetic pressure. The conservation law (2.1) is exact and should be valid for stationary and time-dependent fields as well. In a one-dimensional stationary shock it reduces to

$$\sum_s P_{s,ix} + \frac{B^2 \delta_{ix}}{8\pi} - \frac{B_i B_x}{4\pi} = Q_i = \text{const.}, \tag{2.5}$$

throughout the shock. Here the shock normal is chosen to be along the x -axis. In particular, the magnetic field magnitude should satisfy the pressure balance equation

$$\sum_s P_{s,xx} + \frac{B^2}{8\pi} = \sum_s n_{s,u} m_s V_u^2 + \sum_s n_{s,u} T_{s,u} + \frac{B_u^2}{8\pi}. \tag{2.6}$$

Here, subscript u denotes upstream and we assumed upstream thermal distributions for all species. The equation is written in the normal incidence frame (NIF) where

the upstream plasma velocity is along the shock normal and equal to V_u . Accordingly, the upstream velocities of all species are also V_u along the shock normal.

Following the described separation of the fields we shall treat the magnetic field variations at spatial scales substantially less than the proton inertial length, $\lesssim(c/\omega_{pp})$, and/or at a temporal scale substantially less than the inverse proton gyrofrequency, $\lesssim(1/\Omega_p)$, as fast-varying fields. The only exception is the magnetic ramp whose width may be less than (c/ω_{pp}) since it is the main magnetic jump in the shock. Here $\omega_{pp}^2 = 4\pi n_u e^2/m_p$ and $\Omega_p = eB_u/m_p c$, where the subscript u refers to the asymptotically uniform upstream region. The fast-varying fields affect electron motion strongly (Wilson *et al.* 2012, 2014a,b). However, for any ion species they play the role of weak scattering only. Indeed, the relative momentum change during an ion passing through such a small-scale fluctuation is $\Delta p/p \sim (FL/v)/p$, where F is the force acting on the ion within the fluctuation, L is the typical scale of it and v is the typical ion speed. It is easy to see that the relative change due to the electric field is of the order of $e\varphi/mV^2$, where $\varphi \sim EL$ is the ‘cross-fluctuation’ potential. As long as this potential is a tiny fraction of the ion kinetic energy, the ion experiences only a small kick upon interaction with this field. Similarly, for the magnetic effect we will have a relative change of at most $\tau\Omega_p$ where τ is the crossing time of the small-scale feature. Since $\tau \ll 1/\Omega_p$, the relative change is small. If the fluctuations are bipolar (Wilson *et al.* 2010, 2014c), the relative change on a large number of fluctuations will be quadratic on the smallness parameter. Thus, the fast-varying fluctuations play the role of effective scattering for ions and the mean free path of this scattering exceeds by far the region of the size of several ion convective gyroradii, $r_g = V_u/\Omega_p$, around the ramp. It is this region we are focused on.

The conservation laws (2.1) include both slow and fast variations. In what follows we restrict ourselves to the xx -component only as the most important since the momentum is carried along the shock normal and for simplicity we assume dependence on t and x only. Averaging over fast variations one gets

$$\frac{\partial}{\partial t} \left(\sum_s n_s m_s V_{s,x} \right) + \frac{\partial}{\partial x} \left(P_e + \sum_s P_{s,xx} + \frac{B^2}{8\pi} \right) = 0, \quad (2.7)$$

where on the left-hand side now only slowly varying quantities are retained. The contribution of the fast-varying fields is taken into account by excluding electrons from the kinetic description and using a hydrodynamical equation of state for them. Equation (2.7) describes non-stationarity of macroscopic fields together with ion distributions produced by these macroscopic fields, while the electron pressure P_e absorbs the contribution of the fast-varying fields. Summation is now over ion species only. The strength of deviations from stationarity can be now estimated by verification of the validity of (2.5). This is the objective of the forthcoming sections.

3. Hybrid simulation

We start with a hybrid simulation of a supercritical shock. The simulation is done using the *dHybrid* code (Gargaté *et al.* 2007; Caprioli & Spitkovsky 2014). The simulation is in the plane x - z , with a box size $L_x \times L_z = 80(c/\omega_{pp}) \times 1(c/\omega_{pp})$ and grid spacing of $\Delta x = \Delta z = 0.1(c/\omega_{pp})$. Periodic boundary conditions are imposed across the box. Along the box one side is a reflecting wall and the other side is open, with a constant injection of particles. The small perpendicular size of the box allows us to focus on the time dependence of the shock. Larger widths would be

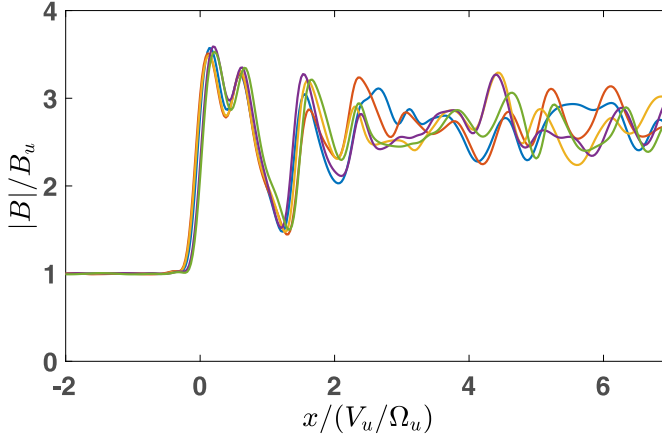


FIGURE 2. Magnetic field: hybrid simulation.

required to include also the effects of rippling, which latter is expected to develop at higher Mach number (Ofman & Gedalin 2013a). For the parameters chosen in this study, rippling is negligible (Ofman *et al.* 2019) and use of a narrow simulation box is justified. The upstream magnetic field is in the simulation plane and the angle is $\theta_{Bn} = 70^\circ$. Two ion species, protons and alpha particles, are treated within the particle-in-cell approach, while electrons are treated as a massless neutralizing fluid with a polytropic state equation $P_e/n_e^\gamma = \text{const.}$, $\gamma = 5/3$. There are 64 particles per cell (p.p.c.) for each species and $n_{\alpha u}/n_{pu} = 0.05$. Increase or decrease of the p.p.c. by a factor of two has not shown any noticeable changes except rapid increase of lapse time for larger p.p.c. numbers. The time step is $0.0025(1/\Omega_p)$ and the system is run for $60/\Omega_p$. The proton Alfvén speed is defined as $v_{pA}^2 = B_u^2/4\pi n_{pu}m_p$, where m_p is the proton mass. All speeds are defined in terms of the proton Alfvén speed, so that the Mach number is V_u/v_{pA} , where V_u is the plasma flow speed in the normal incidence frame (shock frame). Accordingly, the injection speed $v_{in} = 2.5$. Temperature ratios in the solar wind vary in a wide range (Wilson *et al.* 2018). In the present simulations we choose the thermal speeds of both species equal $v_{T\alpha} = v_{Tp} = 0.4$. The electron temperature is $T_e = 0.2(m_p v_{pA}^2/2)$. Thermal parameters are often expressed in terms of $\beta = 8\pi n_p T/B_u^2$, $\beta_i = 2v_{Ti}^2$, $i = p, \alpha$ and $\beta_e = 2T_e$. The total upstream thermal pressure is $n_e T_e + n_p T_p + n_\alpha T_\alpha$, where $n_e = n_p + 2n_\alpha$, which gives $\beta_u \approx 0.7$. It is worth noting that the true MHD (magnetohydrodynamical) Alfvén speed is $v_A^2 = B_u^2/4\pi(n_{pu}m_p + n_{Au}m_A) = v_{pA}^2(1 + 4n_{Au}/n_{pu})$. Therefore, the MHD Mach number is $M_A = M\sqrt{1.2} \approx 1.1M$.

dHybrid applies 3-point averaging which effectively damps all small-scale and high-frequency fluctuations, so that only macroscopic fields remain in the simulation. The macroscopic magnetic fields is time dependent, as is seen from figure 2, where several magnetic profiles averaged across the z -direction of the simulation box are shown. The temporal separation between subsequent profiles is $\Delta t = 2.5/\Omega_p$. They are shifted by $v_{sh}\Delta t$ where the average shock speed is found to be $v_{sh} = 1.16$, which gives the Mach number of the shock of $M = 3.66$ (compare to Ofman *et al.* (2019), who forgot to add the shock speed to the injection speed). The profiles do not coincide completely which means that the shock speed measured by the ramp position is not constant. In other words, the ramp position is time dependent in the shock frame and weakly

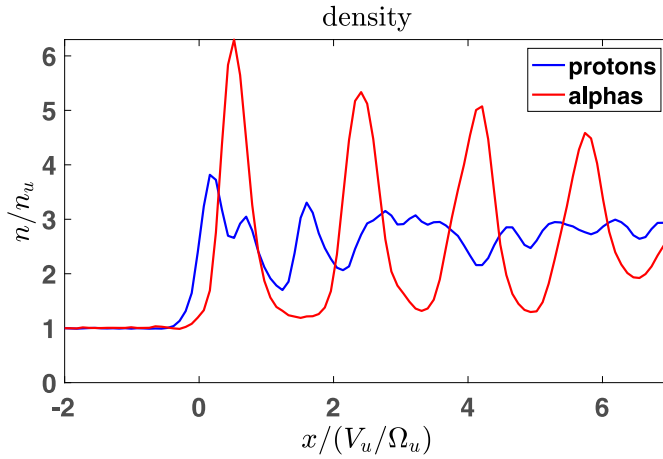


FIGURE 3. Proton (blue) and alpha-particle (red) density evolution throughout the shock (hybrid simulation).

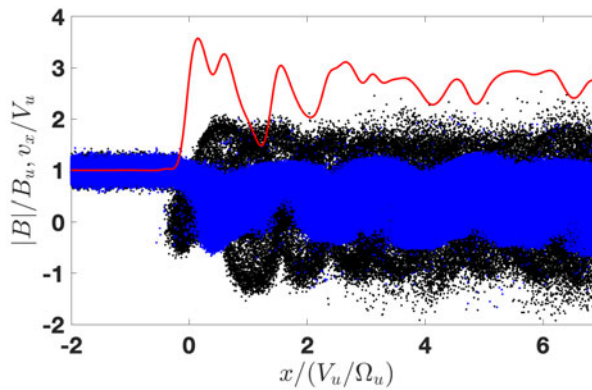


FIGURE 4. Orbits $x-v_x$ of protons (black) and alpha particles (blue) throughout the shock (hybrid simulation). The magnetic field profile is shown in red.

oscillates. Such weak time dependence of moderately supercritical shocks has been found recently in other hybrid simulations (Gedalin 2019a; Ofman *et al.* 2019). It is worth noting that hybrid simulations show that shock formation and stable existence do not require the presence of microscopic fields (Burgess, Wilkinson & Schwartz 1989; Schkopke *et al.* 1990; Scholer & Matsukiyo 2004; Moullard *et al.* 2006; Burgess & Scholer 2007; Scholer & Burgess 2007; Comișel *et al.* 2011; Ofman & Gedalin 2013a,b; Gedalin 2019a; Ofman *et al.* 2019). The macroscopic fields dominate ion motion and ion distribution formation. These distributions, in turn, shape the shock profile.

Figure 3 shows the proton and alpha particle densities in the shock front as obtained in the hybrid simulation. The densities of the species are normalized to their upstream densities. The density oscillations were misinterpreted as surfing (Ofman *et al.* 2019) while in fact they are only a manifestation of ion gyration, as seen in figure 4. The orbits and the density oscillations are very similar to what occurs in low Mach

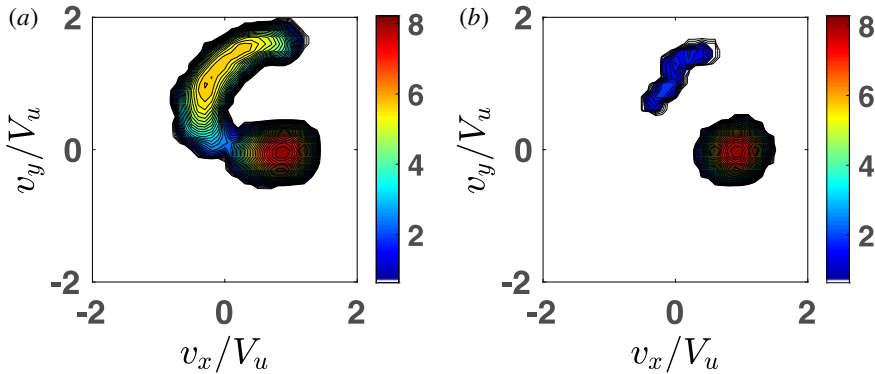


FIGURE 5. Proton (a) and alpha particle (b) distributions in the plane v_x – v_y within the ramp (hybrid simulation).

number shocks and have been comprehensively explained by the theory of kinematic collisionless relaxation (Balikhin *et al.* 2008; Ofman *et al.* 2009; Ofman & Gedalin 2013b; Gedalin 2015; Gedalin, Friedman & Balikhin 2015; Gedalin 2016, 2017; Pope, Gedalin & Balikhin 2019). Surfing or multiple reflection (Lee, Shapiro & Sagdeev 1996; Zank *et al.* 1996) require that ions stay for a large number of gyroperiods in the vicinity of the ramp, while here all ions proceed further downstream immediately. Reflected ions are clearly seen in figure 4 which supports the conclusion that the shock is supercritical. In addition, figure 5 shows the gyrophase bunched distributions of reflected ions inside the ramp. The MHD Alfvén Mach number for this shock is $M_A = 4$. The fast magnetosonic Mach number is $M_F \approx 3.2$ while the critical fast Mach number is $M_c = 2.54$.

4. Ion tracing in the numerically obtained fields

The simulated shock is non-stationary. In order to quantify this effect, we perform ion tracing in the fields found in the simulation at $t = 50/\Omega_u$ as if these fields were time independent. The shock angle, the Mach number and the temperatures of the incident populations are identical to those in the hybrid simulation. The tracing provides distributions of protons and alpha particles throughout the shock which allows us to calculate P_{xx} and derive the magnetic field from the pressure balance (2.5). The derived magnetic field is further compared to the simulated magnetic field. The cross-shock electric field used in the analysis is shown in figure 6. Figure 7 presents a comparison of the magnetic field magnitude found in the hybrid simulation (blue curve) with the magnetic field magnitude calculated from the pressure balance (2.5) (red curve) with the ion distributions found with tracing in static fields. The two magnetic profiles agree much better than could be expected given that the shock was found to be non-stationary in the hybrid simulation. The differences are minor, which means that pressure balance is nearly maintained throughout the shock front.

Figure 8 shows the orbits x – v_x of approximately 80 particles of each species. The orbits are derived as if the numerically found fields were static. This figure should be compared with figure 4. In both cases the orbits clearly show identical maxima and minima and correlation of local maxima of velocity and minima of the magnetic fields, as required by the pressure balance (Gedalin 2015; Gedalin *et al.* 2015).

Distributions of protons (a) and alpha particles (b) inside the ramp, as obtained with ion tracing in the numerically found fields, are shown in figure 9. The distributions

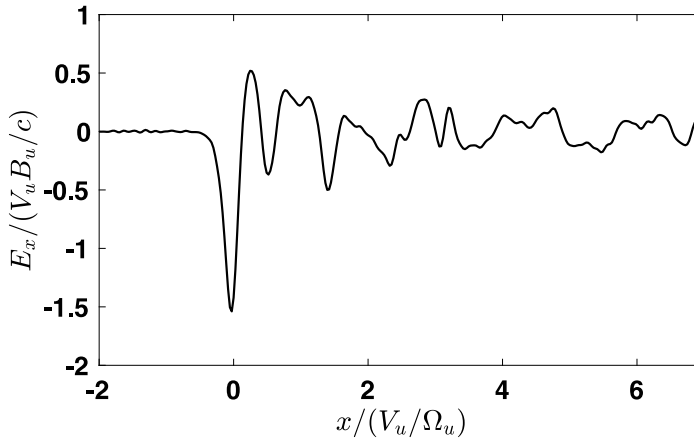


FIGURE 6. Cross-shock electric field found in the hybrid simulation and used in the test particle analysis.

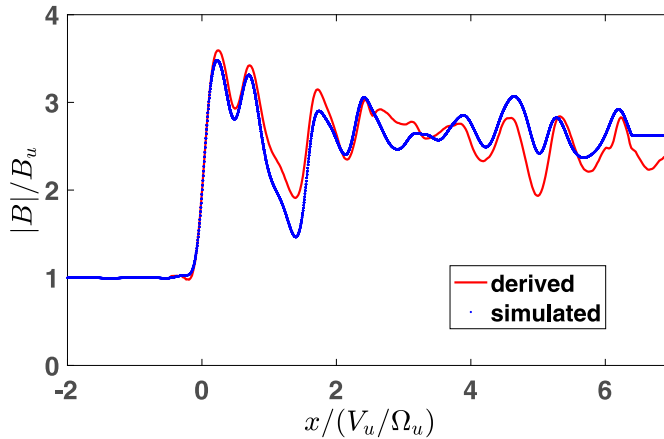


FIGURE 7. Magnetic field from hybrid simulation (blue) versus magnetic field from pressure balance with ion tracing in the simulated fields (red).

are produced in different ways in the hybrid simulations and in the ion tracing. In the hybrid simulations a snapshot at some moment provides velocities of all particles inside the box and the distribution is built afterwards. In the ion tracing an ion contributes each time it crosses the region of interest (the staying time method). The time step is very small. As a result, the effective number of particles is too large to output the velocities, so that the distribution is constructed during the tracing. The similarity of the distributions obtained in the ion tracing (figure 9) and those obtained in the hybrid simulation (figure 5) is better than could be expected taking into account the shock non-stationarity. The last two figures indicate that weak time dependence of the macroscopic fields produces only minor effects on particle distributions.

5. Model fields

The ion tracing above has been performed in the numerically found fields assuming that they are not time dependent. Although these fields are non-stationary, as became

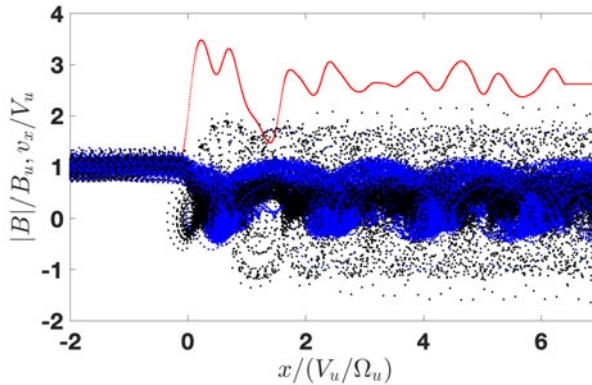


FIGURE 8. Orbits $x-v_x$ of protons (black) and alpha particles (blue) throughout the shock, as derived from ion tracing in the numerically found fields if assumed static. The magnetic field profile is shown in red.

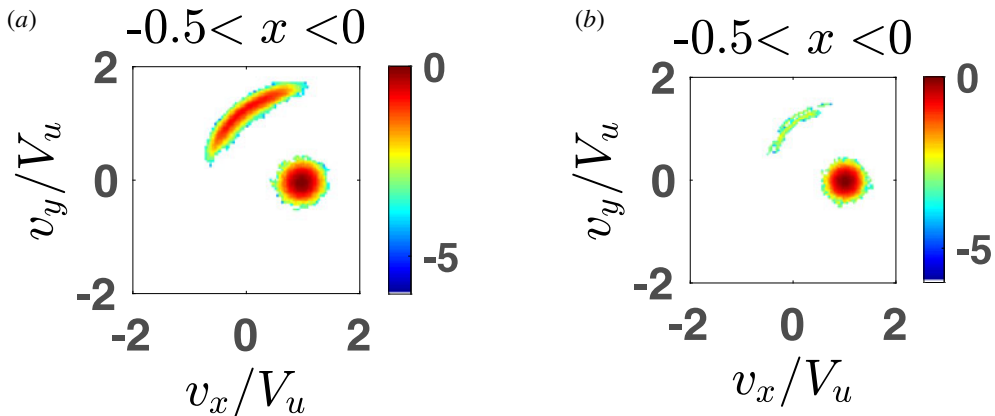


FIGURE 9. Distributions within the ramp obtained by ion tracing in the numerically found fields with the assumption that they are stationary. (a) Protons. (b) Alpha particles.

clear from the hybrid simulation, some agreement could be expected when comparing the numerically found magnetic field with the field which would be consistent with ion dynamics in the stationary fields. The found agreement appeared to be much better than expected. We proceed further by replacing the numerically found fields with model stationary fields. We trace ions in these fields and derive the magnetic field from the pressure balance. The derived field is compared to the field found in the hybrid simulations. In doing so we would be interested in the most simple model which would include a minimum of the details revealed in the hybrid simulation. In earlier works on laminar shocks (Gedalin *et al.* 2015; Gedalin 2016, 2017) a monotonic tanh-like magnetic profile was chosen. This was justified since overshoots were weak and their effect on ions at the shock crossing was minor. In supercritical shocks overshoots are substantial. The cross-shock potential essentially follows the magnetic profile (Gedalin & Balikhin 2004; Dimmock *et al.* 2012; Gedalin 2017). Ion transmission and reflection are particularly sensitive to the potential drop at

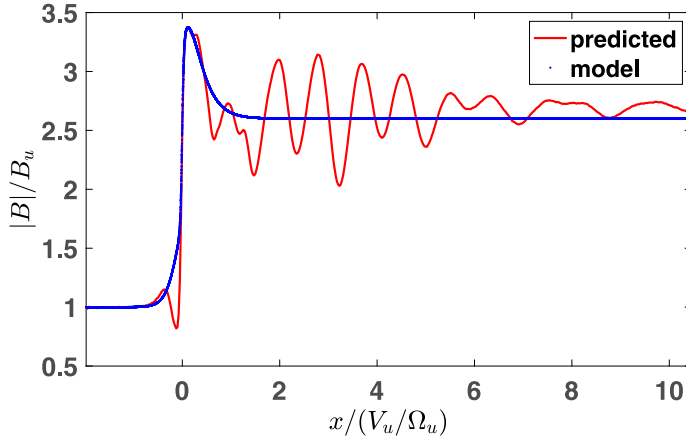


FIGURE 10. Magnetic field: applied analytical model (blue) versus predicted by pressure balance (red).

the ramp (Gedalin 1996, 2016). In the presence of an overshoot the cross-ramp potential may significantly differ from the total cross-shock potential, the latter being measured between the asymptotic uniform upstream and downstream states. We therefore include the overshoot in the model magnetic field discarding the rest of the downstream magnetic oscillations. The model is described using the following analytical expression,

$$B_z = (B_1 + B_2) \sin \theta, \tag{5.1}$$

$$B_1 = 1 + (R - 1)S \left(\frac{3x}{D} \right), \tag{5.2}$$

$$B_2 = B_a \left(\tanh \left(\frac{x - x_l}{W_l} \right) \cdot S \left(\frac{x_r - x}{W_r} \right) + \tanh \left(\frac{x_r - x}{W_r} \right) \cdot S \left(\frac{x - x_l}{W_l} \right) \right), \tag{5.3}$$

$$S(y) \equiv \frac{1}{2}(1 + \tanh y). \tag{5.4}$$

This expression gives a monotonic transition with a smoothly superimposed asymmetric overshoot. The parameters R , D , B_a , x_l , W_l , x_r and W_r allow complete control over the magnetic compression, ramp width, overshoot position and strength and even the rising and descending slopes of the overshoot. The cross-shock electric field is chosen as $E_x \propto dB_z/dz$ with the coefficient of proportionality ensuring that the total normal incidence frame cross-shock potential equals the value found in the simulation. The model non-coplanar magnetic field is also chosen as $B_y \propto dB_z/dx$ with the coefficient of proportionality ensuring that the total de Hoffmann–Teller frame cross-shock potential equals the value found in the simulation (Goodrich & Scudder 1984; Schwartz *et al.* 1988). The magnetic profile used in ion tracing is shown in figure 10 (blue curve), which also presents the magnetic field derived from the pressure balance (red). As can be expected, the derived magnetic field differs from the simulated one since only the overshoot is included in the model while the successive large amplitude downstream oscillations are not taken into account. Yet, even this oversimplified model correctly predicts the main features of the magnetic profile, namely, the downstream oscillations are anti-correlated with the pressure and

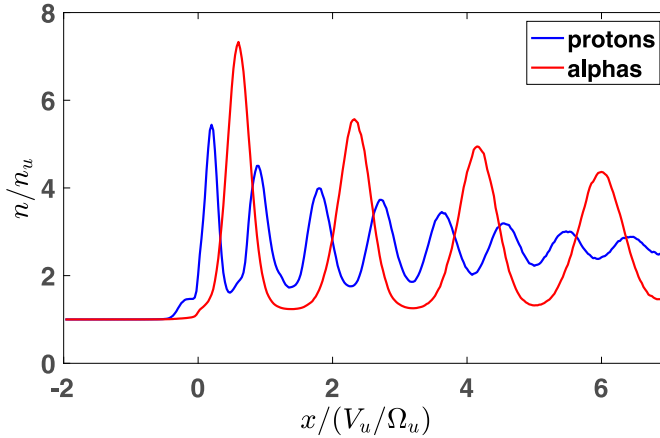


FIGURE 11. Proton (blue) and alpha particle (red) density obtained by ion tracing in the single overshoot model.

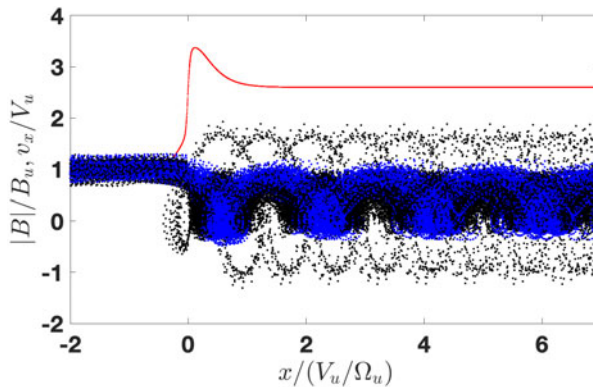


FIGURE 12. Orbits of protons (black) and alpha particles (blue) obtained by ion tracing in the single overshoot model.

there are two kinds of peaks corresponding to the contributions of protons and alpha particles. Comparison of the densities (figure 11 versus figure 3) shows that the densities, especially that of the alpha particles, are less sensitive to the downstream magnetic oscillations than the pressure. This is not surprising since the contribution of the higher energy tail of reflected and quasi-reflected ions is small for density but substantial for pressure. In both simulated and model produced density profiles, spatially damping large-amplitude oscillations are present, with the spatial period for the alpha particles twice as large as for the protons, exactly as expected from gyration and kinematic relaxation. This relaxation is also clearly seen in figure 12 which is to be compared with figure 4 and figure 8. All three show the same pattern of proton and alpha particle orbits. It should be taken into account that only a small part of the orbits is shown for ion tracings while all particles are presented for the hybrid simulation. Thus, figure 8 and figure 12 show sparser distributions than seen in figure 4, yet similar gyration and relaxation are clearly seen in all three.

6. Discussion and conclusions

In the present paper we applied a combined approach to study to what extent a supercritical shock is non-stationary. We started with a self-consistent hybrid simulation of a shock which showed that the shock is non-stationary. The simulations allowed us to evaluate deviations from stationarity by checking the instantaneous pressure balance. The pressure balance would have to be maintained exactly if the shock were planar and time independent. In order to quantify better the deviations, we applied ion tracing across a one-dimensional stationary shock when the magnetic and electric fields of the shock were taken from a single snapshot of the performed hybrid simulation as if they were time independent. The ion distributions throughout the shock were determined and again the pressure balance was exploited, this time to derive the magnetic field which would be consistent with the obtained distributions. Comparison of the derived field with the one used for tracing showed that pressure balance is almost maintained. The pressure imbalance is weak, yet this imbalance is responsible for the temporal variability of the shock behind the ramp. We went even further and compared our hybrid simulations with the results of ion tracing in a completely analytically modelled shock profile, while retaining only the most important feature (overshoot) and the basic shock parameters as in the simulation. Each of these two steps takes us further away from the self-consistent picture obtained within the hybrid simulation. Therefore one could expect progressively worse agreement between the ion distributions and magnetic fields obtained with tracing and those found in the hybrid simulation. Yet, the agreement remained rather good even for the modelled shocks. Recently, the results of a test particle ion tracing have been compared (Gedalin 2019b) with an observed interplanetary supercritical shock observed by MMS (magnetospheric multiscale mission) on 2018-01-08 (Cohen *et al.* 2019). The comparison has shown good agreement. These findings show that (a) the macroscopic fields play the main role in the formation of downstream ion distributions and the magnetic profile of the shock, (b) the time dependence of the analysed moderately supercritical shock with ion reflection is clear but weak and (c) the shock non-stationarity is directly related to the pressure imbalance. The latter means that, in principle, temporal evolution of the shock profiles may be described within the time-dependent conservation-law approach (to be developed). Applicability of the proposed approach to higher Mach number shocks is yet to be explored.

No new dataset was produced in this study. The magnetic field data were taken from the CLUSTER Science Archive <https://csa.esac.esa.int/csa-web/>. Hybrid simulations have been performed using *dHybrid* code. The wavelet transform used the Wavelab package <https://statweb.stanford.edu/~wavelab/>.

REFERENCES

- BALIKHIN, M. A., ZHANG, T. L., GEDALIN, M., GANUSHKINA, N. Y. & POPE, S. A. 2008 Venus Express observes a new type of shock with pure kinematic relaxation. *Geophys. Res. Lett.* **35**, L01103.
- BURGESS, D. & SCHOLER, M. 2007 Shock front instability associated with reflected ions at the perpendicular shock. *Phys. Plasmas* **14**, 012108.
- BURGESS, D., WILKINSON, W. P. & SCHWARTZ, S. J. 1989 Ion distributions and thermalization at perpendicular and quasi-perpendicular supercritical collisionless shocks. *J. Geophys. Res.* **94**, 8783–8792.
- CAPRIOLI, D. & SPITKOVSKY, A. 2014 Simulations of ion acceleration at non-relativistic shocks. I. Acceleration efficiency. *Astrophys. J.* **783** (2), 91.

- COHEN, I. J., SCHWARTZ, S. J., GOODRICH, K. A., AHMADI, N., ERGUN, R. E., FUSELIER, S. A., DESAI, M. I., CHRISTIAN, E. R., MCCOMAS, D. J., ZANK, G. P. *et al.* 2019 High-resolution measurements of the cross-shock potential, ion reflection, and electron heating at an interplanetary shock by MMS. *J. Geophys. Res.* **90** (A12), 12,095.
- COMIŞEL, H., SCHOLER, M., SOUCEK, J. & MATSUKIYO, S. 2011 Non-stationarity of the quasi-perpendicular bow shock: comparison between Cluster observations and simulations. *Ann. Geophys.* **29**, 263–274.
- CORONITI, F. V. 1970 Dissipation discontinuities in hydromagnetic shock waves. *J. Plasma Phys.* **4**, 265–282.
- DIMMOCK, A. P., BALIKHIN, M. A., KRASNOSELSKIKH, V. V., WALKER, S. N., BALE, S. D. & HOBARA, Y. 2012 A statistical study of the cross-shock electric potential at low Mach number, quasi-perpendicular bow shock crossings using Cluster data. *J. Geophys. Res.* **117**, 02210.
- DIMMOCK, A. P., RUSSELL, C. T., SAGDEEV, R. Z., KRASNOSELSKIKH, V., WALKER, S. N., CARR, C., DANDOURAS, I., ESCOUBET, C. P., GANUSHKINA, N., GEDALIN, M. *et al.* 2019 Direct evidence of nonstationary collisionless shocks in space plasmas. *Sci. Adv.* **5** (2), eaau9926.
- EDMISTON, J. P. & KENNEL, C. F. 1984 A parametric survey of the first critical Mach number for a fast MHD shock. *J. Plasma Phys.* **32** (3), 429–441.
- FARRIS, M., RUSSELL, C. & THOMSEN, M. 1993 Magnetic structure of the low beta, quasi-perpendicular shock. *J. Geophys. Res.* **98**, 15285–15294.
- GARGATÉ, L., BINGHAM, R., FONSECA, R. A. & SILVA, L. O. 2007 dHybrid: A massively parallel code for hybrid simulations of space plasmas. *Comput. Phys. Commun.* **176** (6), 419–425.
- GEDALIN, M. 1996 Ion reflection at the shock front revisited. *J. Geophys. Res.* **101**, 4871–4878.
- GEDALIN, M. 2015 Collisionless relaxation of non-gyrotropic downstream ion distributions: dependence on shock parameters. *J. Plasma Phys.* **81**, 905810603.
- GEDALIN, M. 2016 Transmitted, reflected, quasi-reflected, and multiply reflected ions in low-Mach number shocks. *J. Geophys. Res.* **121**, 10.
- GEDALIN, M. 2017 Effect of alpha particles on the shock structure. *J. Geophys. Res.* **122**, 71–76.
- GEDALIN, M. 2019a Kinematic collisionless relaxation and time dependence of supercritical shocks with alpha particles. *Astrophys. J.* **880**, 140.
- GEDALIN, M. 2019b Kinematic collisionless relaxation of ions in supercritical shocks. *Frontiers in Physics* **7**, 692.
- GEDALIN, M. & BALIKHIN, M. 2004 Electric potential in the low-Mach-number quasi-perpendicular collisionless shock ramp revisited. *J. Geophys. Res.* **109**, 3106.
- GEDALIN, M., FRIEDMAN, Y. & BALIKHIN, M. 2015 Collisionless relaxation of downstream ion distributions in low-Mach number shocks. *Phys. Plasmas* **22**, 072301.
- GEDALIN, M., NEWBURY, J. A. & RUSSELL, C. T. 1998 Shock profile analysis using wavelet transform. *J. Geophys. Res.* **103** (A4), 6503–6512.
- GEDALIN, M., NEWBURY, J. A. & RUSSELL, C. T. 2000 Numerical analysis of collisionless particle motion in an observed supercritical shock front. *J. Geophys. Res.* **105** (A), 105–114.
- GOODRICH, C. C. & SCUDDER, J. D. 1984 The adiabatic energy change of plasma electrons and the frame dependence of the cross-shock potential at collisionless magnetosonic shock waves. *J. Geophys. Res.* **89**, 6654–6662.
- GRANIT, G. & GEDALIN, M. 2018 Whistler precursor and intrinsic variability of quasi-perpendicular shocks. *J. Plasma Phys.* **84** (1), 905840113.
- GREENSTADT, E. W., SCARF, F. L., RUSSELL, C. T., FORMISANO, V. & NEUGEBAUER, M. 1975 Structure of the quasi-perpendicular laminar bow shock. *J. Geophys. Res.* **80**, 502.
- GREENSTADT, E. W., SCARF, F. L., RUSSELL, C. T., GOSLING, J. T., BAME, S. J., PASCHMANN, G., PARKS, G. K., ANDERSON, K. A., ANDERSON, R. R. & GURNETT, D. A. 1980 A macroscopic profile of the typical quasi-perpendicular bow shock - I see 1 and 2. *J. Geophys. Res.* **85**, 2124–2130.
- KAJDIČ, P., BLANCO-CANO, X., AGUILAR-RODRIGUEZ, E., RUSSELL, C. T., JIAN, L. K. & LUHMANN, J. G. 2012 Waves upstream and downstream of interplanetary shocks driven by coronal mass ejections. *J. Geophys. Res.* **117**, A06103.
- KENNEL, C. F. 1987 Critical Mach numbers in classical magnetohydrodynamics. *J. Geophys. Res.* **92**, 13427–13437.

- KRASNOSELSKIKH, V., LEMBÈGE, B., SAVOINI, P. & LOBZIN, V. 2002 Nonstationarity of strong collisionless quasiperpendicular shocks: theory and full particle numerical simulations. *Phys. Plasmas* **9**, 1192.
- KUMAR, P. & FOUFOULA-GEORGIOU, E. 1997 Wavelet analysis for geophysical applications. *Rev. Geophys.* **35**, 385–412.
- LEE, M. A., SHAPIRO, V. D. & SAGDEEV, R. Z. 1996 Pickup ion energization by shock surfing. *J. Geophys. Res.* **101**, 4777.
- LEMBÈGE, B., SAVOINI, P., HELLINGER, P. & TRÁVNÍČEK, P. M. 2009 Nonstationarity of a two-dimensional perpendicular shock: competing mechanisms. *J. Geophys. Res.* **114**, 3217.
- LOBZIN, V. V., KRASNOSELSKIKH, V. V., BOSQUED, J.-M., PINÇON, J.-L., SCHWARTZ, S. J. & DUNLOP, M. 2007 Nonstationarity and reformation of high-Mach-number quasiperpendicular shocks: cluster observations. *Geophys. Res. Lett.* **34**, 05107.
- LOBZIN, V. V., KRASNOSELSKIKH, V. V., MUSATENKO, K. & DE WIT, T. D. 2008 On nonstationarity and rippling of the quasiperpendicular zone of the Earth bow shock: cluster observations. *Ann. Geophys.* **26**, 2899.
- MAZELLE, C., LEMBÈGE, B., MORGENTHALER, A., MEZIANE, K., HORBURY, T. S., GÉNOT, V., LUCEK, E. A., DANDOURAS, I., MAKSIMOVIC, M., ISSAUTIER, K. *et al.* 2010 Self-reformation of the quasi-perpendicular shock: CLUSTER observations. In *Twelfth International Solar Wind Conference*, pp. 471–474. AIP.
- MELLOTT, M. M. & GREENSTADT, E. W. 1984 The structure of oblique subcritical bow shocks - ISEE 1 and 2 observations. *J. Geophys. Res.* **89**, 2151–2161.
- MOULLARD, O., BURGESS, D., HORBURY, T. S. & LUCEK, E. A. 2006 Ripples observed on the surface of the Earth's quasi-perpendicular bow shock. *J. Geophys. Res.* **111**, 10.
- NEWBURY, J. A., RUSSELL, C. T. & GEDALIN, M. 1998 The ramp widths of high-Mach-number, quasi-perpendicular collisionless shocks. *J. Geophys. Res.* **103** (A), 29581–29594.
- NEWBURY, J. A., RUSSELL, C. T. & GEDALIN, M. 1998 The ramp widths of high-Mach-number, quasi-perpendicular collisionless shocks. *J. Geophys. Res.* **103**, 29581–29594.
- OFMAN, L., BALIKHIN, M., RUSSELL, C. T. & GEDALIN, M. 2009 Collisionless relaxation of ion distributions downstream of laminar quasi-perpendicular shocks. *J. Geophys. Res.* **114**, 09106.
- OFMAN, L. & GEDALIN, M. 2013a Rippled quasi-perpendicular collisionless shocks: local and global normals. *J. Geophys. Res.* **118**, 5999–6006.
- OFMAN, L. & GEDALIN, M. 2013b Two-dimensional hybrid simulations of quasi-perpendicular collisionless shock dynamics: gyrating downstream ion distributions. *J. Geophys. Res.* **118**, 1828–1836.
- OFMAN, L., KOVAL, A., WILSON, L. B. III & SZABO, A. 2019 Understanding the role of α particles in oblique heliospheric shock oscillations. *J. Geophys. Res.* **82** (4), 905820401–13.
- POPE, S. A., GEDALIN, M. & BALIKHIN, M. A. 2019 The first direct observational confirmation of kinematic collisionless relaxation in very-low Mach number shocks near the earth. *J. Geophys. Res.* **165**, 3–15.
- RUSSELL, C., HOPPE, M., LIVESEY, W. & GOSLING, J. 1982 Isee-1 and- 2 observations of laminar bow shocks- velocity and thickness. *Geophys. Res. Lett.* **9**, 1171.
- SCHOLER, M. & BURGESS, D. 2007 Whistler waves, core ion heating, and nonstationarity in oblique collisionless shocks. *Phys. Plasmas* **14**, 072103.
- SCHOLER, M. & MATSUKIYO, S. 2004 Nonstationarity of quasi-perpendicular shocks: a comparison of full particle simulations with different ion to electron mass ratio. *Ann. Geophys.* **22**, 2345–2353.
- SCHWARTZ, S. J., THOMSEN, M. F., BAME, S. J. & STANSBERRY, J. 1988 Electron heating and the potential jump across fast mode shocks. *J. Geophys. Res.* **93**, 12923–12931.
- SCKOPKE, N., PASCHMANN, G., BRINCA, A. L., CARLSON, C. W. & LUEHR, H. 1990 Ion thermalization in quasi-perpendicular shocks involving reflected ions. *J. Geophys. Res.* **95**, 6337–6352.
- SCUDDER, J. D., AGGSON, T. L., MANGENEY, A., LACOMBE, C. & HARVEY, C. C. 1986 The resolved layer of a collisionless, high beta, supercritical, quasi-perpendicular shock wave. I - Rankine-Hugoniot geometry, currents, and stationarity. *J. Geophys. Res.* **91**, 11019–11052.
- TORRENCE, C. & COMPO, G. P. 1998 A practical guide to wavelet analysis. *Bull. Am. Meteorol. Soc.* **79**, 61.

- UMEDA, T., KIDANI, Y., YAMAO, M., MATSUKIYO, S. & YAMAZAKI, R. 2010 On the reformation at quasi- and exactly perpendicular shocks: full particle-in-cell simulations. *J. Geophys. Res.* **115**, A10250.
- WILSON, L. B., SIBECK, D. G., BRENEMAN, A. W., CONTEL, O. L., CULLY, C., TURNER, D. L., ANGELOPOULOS, V. & MALASPINA, D. M. 2014a Quantified energy dissipation rates in the terrestrial bow shock: 1. Analysis techniques and methodology. *J. Geophys. Res.* **119**, 6455–6474.
- WILSON, L. B., SIBECK, D. G., BRENEMAN, A. W., CONTEL, O. L., CULLY, C., TURNER, D. L., ANGELOPOULOS, V. & MALASPINA, D. M. 2014b Quantified energy dissipation rates in the terrestrial bow shock: 2. Waves and dissipation. *J. Geophys. Res.* **119** (8), 6475–6495.
- WILSON, L. B., SIBECK, D. G., BRENEMAN, A. W., CONTEL, O. L., CULLY, C., TURNER, D. L., ANGELOPOULOS, V. & MALASPINA, D. M. 2014c Quantified energy dissipation rates in the terrestrial bow shock: 2. Waves and dissipation. *J. Geophys. Res.* **119** (8), 6475–6495.
- WILSON, L. B. I., CATTELL, C. A., KELLOGG, P. J., GOETZ, K., KERSTEN, K., KASPER, J. C., SZABO, A. & WILBER, M. 2010 Large-amplitude electrostatic waves observed at a supercritical interplanetary shock. *J. Geophys. Res.* **115** (A), A12104.
- WILSON, L. B. I., KOVAL, A., SZABO, A., BRENEMAN, A., CATTELL, C. A., GOETZ, K., KELLOGG, P. J., KERSTEN, K., KASPER, J. C., MARUCA, B. A. *et al.* 2012 Observations of electromagnetic whistler precursors at supercritical interplanetary shocks. *Geophys. Res. Lett.* **39**, L08109.
- WILSON, L. B. I., STEVENS, M. L., KASPER, J. C., KLEIN, K. G., MARUCA, B. A., BALE, S. D., BOWEN, T. A., PULUPA, M. P. & SALEM, C. S. 2018 The statistical properties of solar wind temperature parameters near 1 au. *Astrophys. J. Suppl. Series* **236** (2), 41.
- WILSON, L. B. III, KOVAL, A., SZABO, A., STEVENS, M. L., KASPER, J. C., CATTELL, C. A. & KRASNOSELSKIKH, V. V. 2017 Revisiting the structure of low-Mach number, low-beta, quasi-perpendicular shocks. *J. Geophys. Res.* **81**, 2097.
- YANG, Z. W., LU, Q. M., LEMBÈGE, B. & WANG, S. 2009 Shock front nonstationarity and ion acceleration in supercritical perpendicular shocks. *J. Geophys. Res.* **114**, 03111.
- ZANK, G., PAULS, H., CAIRNS, I. & WEBB, G. 1996 Interstellar pickup ions and quasi-perpendicular shocks: implications for the termination shock and interplanetary shocks. *J. Geophys. Res.* **101**, 457.